Nano Energy 66 (2019) 104178

Contents lists available at ScienceDirect

Nano Energy

journal homepage: http://www.elsevier.com/locate/nanoen

Full paper

Encapsulating lithium and sodium inside amorphous carbon nanotubes through gold-seeded growth

Xiangna Lan [a], Weibin Ye [a], Hongfei Zheng [a], Yong Cheng [a], Qiaobao Zhang [a], Dong-Liang Peng [a], Ming-Sheng Wang [a,b,*]

[a] Department of Materials Science and Engineering, College of Materials, Xiamen University, Xiamen, Fujian, 361005, China
[b] Pen-Tung Sah Institute of Micro-Nano Science and Technology, Xiamen University, Xiamen, Fujian, 361005, China

ARTICLE INFO

Keywords:
Lithium/sodium metal anode
Amorphous carbon nanotube
Au-seeded growth
Spatially confined plating/stripping
In-situ TEM

ABSTRACT

Metallic lithium promises the ultimate anode material for building next-generation Li batteries, though some fundamental hurdles remain unsolved. Li growth induced by hetero particles/atoms has recently emerged as a highly efficient route enabling spatial-control and dendrite-free Li deposition on anode hosts. However, the detailed mechanism of Li nucleation and its interaction with heterogeneous seeds are largely unknown. Herein, we investigate this issue by visualizing Au-seeded Li nucleation processes that guide Li deposition inside the one-dimensional hollow space of individual amorphous carbon nanotubes by *in-situ* transmission electron microscopy. A reversible two-step conversion process during Au–Li alloying/dealloying reactions is revealed, suggesting that the formation of Li_3Au plays the actual role in inducing Li nucleation. We propose a front-growth scenario to explain the spatially confined Li growth and stripping kinetic behaviors, which involves the mass addition and removal at the deposition front through ion diffusion along the tubular carbon shell. As a comparison, nanotubes without gold seeds inside exhibit uncontrolled dendrite-like Li growth outside the carbon shell. We further demonstrate that Au-seed growth can be successful in encapsulating sodium metal for the first time. These findings provide mechanistic insights into heterogeneous seeded Li/Na nucleation and space-confined deposition for design of high-performance battery anodes.

1. Introduction

Owing to the highest specific capacity (3860 mA h g^{-1}) and lowest electrochemical potential (−3.04 V vs SHE), lithium metal is believed to be the most promising anode material for building high-energy-density battery systems, such as Li–S and Li–O_2 batteries [1–5]. However, Li metal anodes suffer from several intractable issues, including dendritic lithium growth, unstable Li/electrolyte interface and huge electrode volume change, etc. [6–10] This would result in safety hazard and low cycling efficiency and severely impede the commercialization of Li metal batteries (LMBs). Numerous strategies have been proposed to tackle these problems, for instance, by modifying the liquid electrolytes/additives and employing artificial SEI layers and solid electrolytes, etc. [3, 4, 11–13].

Recent advances in rational design of Li host architectures have attracted considerable attention, because of their advantages in regulating Li deposition and accommodating the tremendous volume change during cycling [8,14–19]. Among the various host architecture designs, a truly attractive design concept is the encapsulation of lithium metal with individual carbon nanocapsules [16,20–22]. Each nanocapsule not only provides a fully enclosed space that isolates the filled Li metal from the outside electrolyte, but stabilizes the as-formed SEI through the mechanically robust carbon shell, thus leading to reduced side reaction and improved cycling stability.

The key for such spatial-control Li deposition is the use of heterogeneous nanoseeds, which can guide Li metal to selectively nucleate and grow inside the nanospheres, as proposed by Cui *et al.* in their pioneering works [20]. Metal nanoparticles (NPs) (such as Au, Ag and Mg) with zero overpotential of Li nucleation have proven effective in directing Li deposition in carbonaceous host materials [2, 20, 22–25]. Recent studies also demonstrated that even single-atom-level doping (with Co, Ni, Zn) could induce preferential Li nucleation, thus facilitating the uniform and dendrite-free deposition in carbon matrices [26, 27]. Despite the substantial progress and growing interest in hetero-particle/atom guided Li

* Corresponding author. Department of Materials Science and Engineering, College of Materials, Xiamen University, Xiamen, Fujian, 361005, China.
E-mail address: mswang@xmu.edu.cn (M.-S. Wang).

https://doi.org/10.1016/j.nanoen.2019.104178
Received 10 September 2019; Received in revised form 2 October 2019; Accepted 6 October 2019
Available online 10 October 2019
2211-2855/

deposition, little work has focused on Li metal nucleation and growth behaviors as well as their detailed interaction with the heterogeneous seeds during repeated cycling. In particular, the spatially confined environment built in individual nanocapsules may significantly change the reaction kinetic behaviors. However, relevant information remains largely unknown, due primarily to the lack of direct observation of these processes.

In this contribution, *in situ* transmission electron microscope (TEM) approaches are used to directly visualize the Au-seeded Li/Na plating/stripping behaviors within a confined space. We construct a nanobattery system by adopting amorphous carbon nanotube embedded with gold NPs (Au@aCNTs) as the electrochemical reaction nanocontainers. Different from the nanospheres used in previous works, these nanotubes each provide a one-dimensional hollow space, which facilitates the tracking of Li deposition fronts and the analysis of its growth dynamics. The in-situ TEM observation of the reaction kinetic processes allow some critical information to be revealed with emphasis on: (1) the role of Au NPs in directing Li deposition, and their exact phase and morphological changes in the reaction with Li; (2) Li plating/stripping dynamics and its relationship with Li-ion transport pathways in the tubular carbon shell; (3) the influence of shell confinement on the Au-seeded Li nucleation and growth behaviors. In addition, the encapsulation of sodium through Au-seeded growth was successfully attempted for the first time. Our findings can provide valuable insights for in-depth understanding of the controlled Li/Na deposition assisted by heterogeneous seeds, which would be critical for design of advanced host architectures for high-performance Li/Na metal anodes.

2. Results and discussion

The main idea of the host design is the use of gold nanoparticles loaded inside the hollow amorphous carbon nanotubes to induce Li deposition in the void spaces, as shown in Fig. 1a. Fig. 1b illustrates the synthetic procedure of Au@aCNTs starting from ZnO nanowires as the template. After modifying ZnO nanowires (1–2 μm in length and 50–100 nm in diameter) with 3-aminopropyltriethoxysilane, citrate-stabilized Au NPs (10–20 nm) were immobilized onto the surface of ZnO nanowires. Afterwards, Au@ZnO was conformally coated with a resorcinol formaldehyde (RF) resin, followed by a carbonization process under Ar_2 atmosphere. Due to the porous nature of the amorphous carbon (a-C) shells, the ZnO template can be removed simply by HCl etching, resulting in hollow aCNTs with Au NPs inside. The hollow amorphous CNTs without Au NPs (Fig. 1c) were also prepared in a similar procedure for the control experiments (see Fig. 5e–i).

The as-prepared Au@aCNTs have a carbon shell of about 20 nm thick, which can offer a robust support for the hollow architecture (Fig. 1d). The a-C shell with partially graphitized grains (see Fig. S1) has enhanced electronic conductivity as well as enough conducting channels for both Li and Na ions [28, 29]. The Au NPs distribution inside the hollow carbon nanotubes can be clearly seen in both HADDF (Fig. 1e)

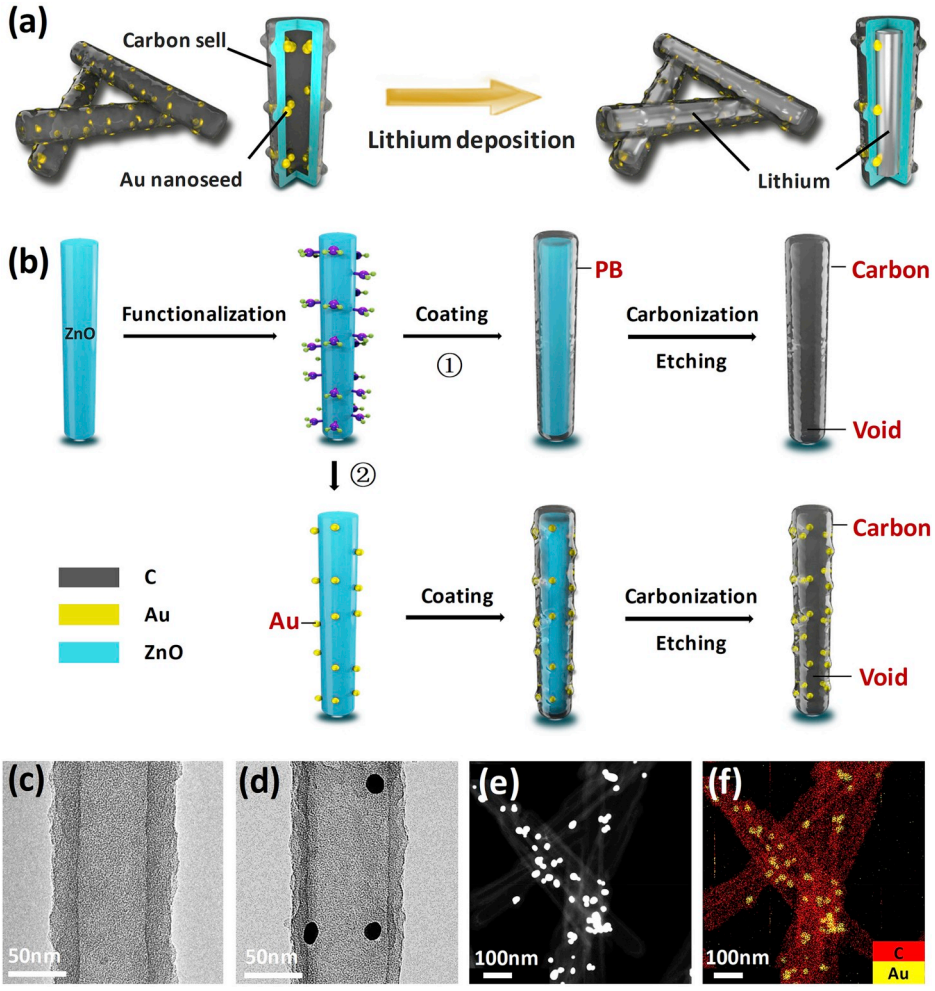

Fig. 1. Synthesis and characterization of Au@aCNTs and aCNTs. (a) Schematic of Li encapsulation inside Au@aCNTs. (b) Synthesis procedure of Au@aCNTs and aCNTs. (c) TEM image of a typical aCNT. (d) TEM image of a typical Au@aCNT. Au NPs inside are visible with dark contrast. (e, f) HADDF image and corresponding EDS element map of Au@aCNTs.

and EDS mapping (Fig. 1f) images with sharp contrast between Au and carbon. It should be pointed out that most of the Au NPs are embedded within the carbon shell (as illustrated in Fig. 2e, g), rather than attached on it inner surface.

In-situ Li plating/stripping experiments were performed inside a TEM equipped with a STM holder that allows for in-situ construction of a dry-cell nanobattery. A tungsten tip loaded with Li metal, together with its surface Li_2O layer (as a solid electrolyte), works as a movable electrode, as described in Fig. S2 and our previous works [30,31]. After the contact was established between Au@aCNTs and a Li_2O/Li electrode, a bias of 3 V/-3 V was applied across them to initiate the reactions. Fig. 2 presents the Li plating/stripping processes of a single Au@aCNT in the first two cycles. Morphological changes were first observed at the Au particle 1 as indicated in Fig. 2a_1. It expanded slightly upon the alloying reaction with Li in the early stage (Fig. 2a_2). Apparently, Li ions required for the reaction should be supplied through ion transport along the carbon shell toward the particle. Further lithiation led to a huge volume expansion of the alloyed particle, followed by Li nucleation on its surface (Fig. 2a_3). Starting from this Li nucleus, Li metal grew both upward and downward and rapidly filled up the hollow cavity of the nanotube, with the fully-alloyed Au seed immersed in the Li deposit (Fig. 2a_4). (See Fig. S3 for more details of the downward growth of Li inside another Au@aCNT.)

One may note that the particle 1 shows obvious morphological

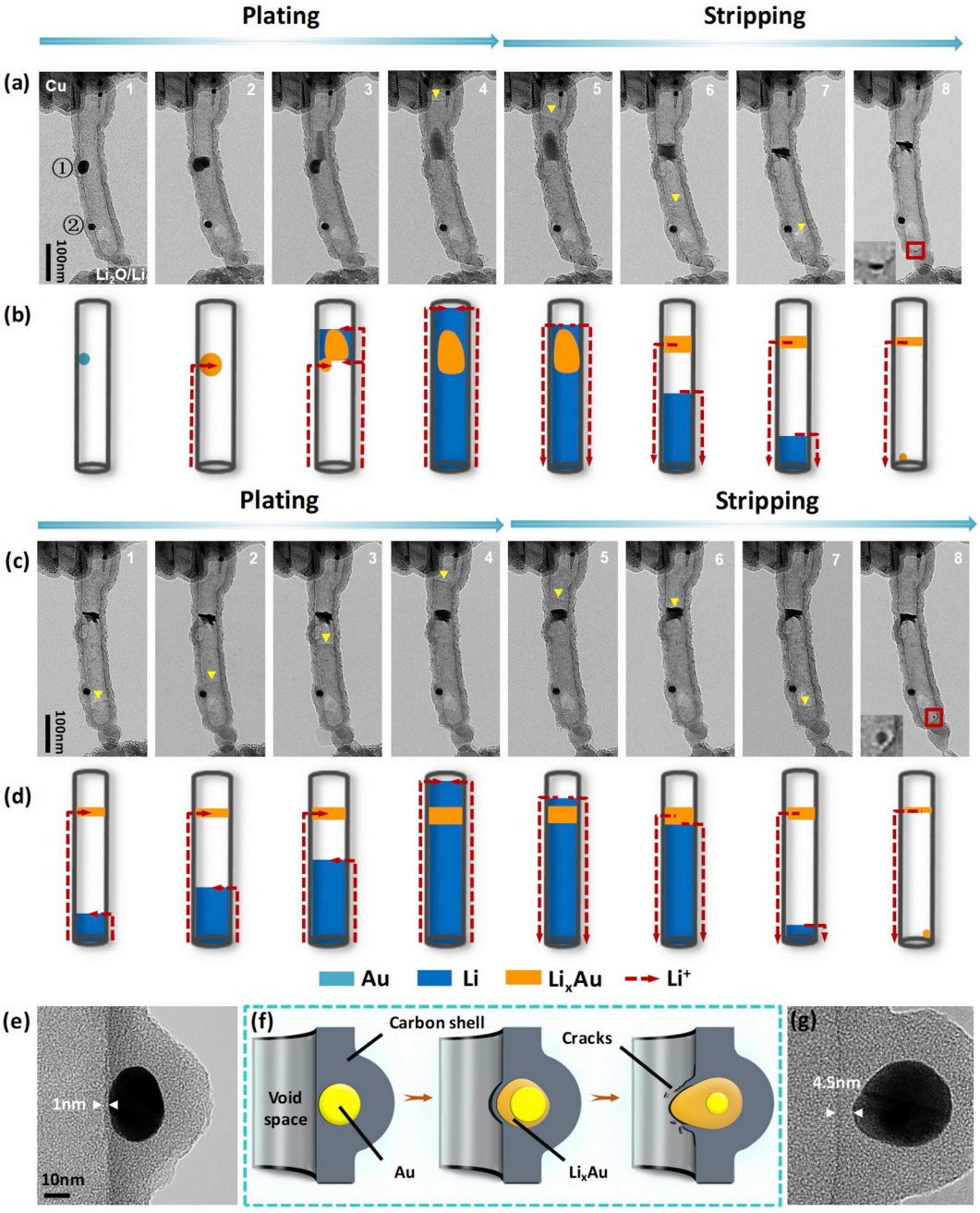

Fig. 2. Encapsulation of lithium metal in an Au@aCNT. TEM snapshots and corresponding schematics showing the Li deposition/stripping processes inside an Au@aCNT during the first (a, b) and second (c, d) cycles. The deposition fronts are highlighted with yellow arrowheads in a, c, and the ion transport paths are indicated by the red dashed arrows in b, d. (e, g) Cross-sectional view of the interface of an Au NP embedded within the carbon shell. The particles are isolated from the inner cavity by a thin (e) or thick (g) carbon layer, as indicated by the arrowheads. (f) Schematic of an embedded Au NP that enters the inner tube space by breaking through the separating layer upon lithiation.

changes, while the particle 2 remains almost unchanged. This can be elucidated by examining the exact shell structures that impose confinement on the particles. The cross-sectional view of the interface between a gold particle and the surrounding shell reveals that there typically exists a very thin layer (~1 nm) separating the particle from the inner tube space (Fig. 2e). Fig. 2f illustrates schematically how a gold particle enters the inner hollow space upon lithiation. In this process, the thin carbon layer can somewhat restrict the particle from expansion and retard the lithiation process until the shell breaks under pressure (this is exactly the case of particle 1, referred to as the "active" particle). However, if the separating layer is too thick (see the example in Fig. 2g) or the particle too small, the particle will be firmly confined inside the carbon shell. The rigid shell confinement can stop the particle from alloying with Li. The particle 2 should belong to this kind of "dead" particles. That is why Li plating started form the particle 1 instead of particle 2, though the latter is closer to the Li/Li_2O electrode.

We next changed the polarity of the applied bias, and accordingly, Li metal was stripped out of the nanotube cavity, as evident from the backward (downward) motion of the deposition front (DF) (marked with the yellow arrowheads in Fig. $2a_{5\text{-}7}$). Along with the volume decrease of Li metal, the alloyed particle was shrinking in size simultaneously. Eventually, the particle was strikingly contracted and exhibited a much darker contrast (Fig. $2a_8$). Diffraction analysis (Fig. 4) shows that the metallic Au phase can reemerge in the dealloying particle at the end of stripping.

It is noteworthy that at the end of this cycle, a tiny cluster was left behind at the bottom of the nanotube, as highlighted in the inset of Fig. $2a_8$. This cluster, around 3 nm in size, is reasonably assumed to be gold or its alloy. It verifies that a minor fraction of Au atoms have dissolved into Li metal at room temperature, as indicated by the binary phase diagram (Fig. S4) [32]. Afterwards, the dissolved Au atoms can precipitate as separate clusters elsewhere apart from the original particle. Interestingly, this newly-formed cluster could significantly change the deposition path in the following cycle, as documented in Fig. 2c. In this cycle, Li nucleated and propagated upward from the bottom of the tube, instead of from the upper particle 1 (Video S1). Note that once Li nucleated, the tiny cluster was instantly dissolved into Li metal and vanished (Fig. $2c_1$). This demonstrates that an Au-rich seed, regardless of its minimal mass, is effective in guiding Li deposition. These results also suggest that the seed closer to Li electrode has higher priority for inducing Li nucleation, due to the shorter ion diffusion distance. The upper particle 1 was lithiated seconds later (before the arrival of the DF), as evidenced by its slight volume expansion (Fig. $2c_{2\text{-}3}$). However, this did not change the growth direction of Li: it propagated upward all the way and submerged the upper Au seed (Fig. $2c_4$). Similar to the first cycle, the following stripping process ended up with the precipitation of a tiny cluster onto the bottom of the tube, but at a slightly changed position (Fig. $2c_8$). This cluster can once again seed the Li growth from the nanotube bottom (not shown).

Supplementary data related to this article can be found at https://doi.org/10.1016/j.nanoen.2019.104178.

As demonstrated above, each plating/stripping cycle can lead to morphological changes and spatial redistribution of Au seeds, which in turn alter the Li plating/stripping behavior of the next cycle. Nevertheless, thanks to the confinement from the tube shells, the Au seeds remain entirely inside the nanotube cavity. Besides, these tubular a-C shells are particularly important for providing the main channels for Li ions to transport in such a spatially confined system. Fig. 2b and d illustrates schematically the proposed Li ion diffusion paths and their relationship with Li metal growth and stripping. Li metal first nucleates on a gold seed with the continuous Li supply through the tube wall. After nucleation, then, there are two possible Li growth scenarios due to the presence of the carbon shell. In the first growth model, the Au seed assists in the incorporation of incoming Li ions into Li crystal at the Au/Li interface, in analogy to a catalytic base-growth process [33, 34]. In the confined space, however, Li ion incorporation at the Au/Li interface has to overcome an extremely large energy barrier imposed by the interaction between the encapsulating shell and the grown Li crystal (especially for a longer one). In the second model, instead, Li ions are directed to the Li deposition front through the carbon shell, leading to Li crystal growth at its front surface (herein referred to as "front-growth", as illustrated by the red dashed arrows in Fig. 2b and d). Obviously, the addition of Li ions at the free surface of growth front would be energetically more favorable than at the Au/Li (or C-shell/Li) interface. In this front-growth scenario, the added Li ions at the front are neutralized by the electrons coming from the counter copper electrode through the nanotube. In addition, once nucleated, Li deposits can propagate even without the Au seed (as the case in Fig. $2c_{1\text{-}4}$), which supports the front growth scenario but not the catalytic one. Likewise, in a stripping process, Li ions are more likely to be removed from the front surface of Li metal, followed by the ion diffusion along the tube shell back to the Li electrode. In this process, the electrons should transport in the opposite direction along the carbon shell toward the counter electrode. Meanwhile, through ion diffusion along the tube shell, Li ions can be extracted from the Li_xAu particle as well, resulting in the observed size shrinking of the particle.

We further demonstrate in Fig. 3 that a longer nanotube over 1.5 μm can be fully filled with Li, where Li propagates from the bottom Au seed and all the way up in the channel. This is another piece of evidence to support the front-growth model, since it imposes less restriction on the Li growth in the longitudinal direction owing to the efficient ion transport in the long a-C shell. Interestingly, once the growing Li reached (or approached) the other end of the nanotube, an electrical breakdown of the nanotube happened due to a short circuit caused by the core Li nanowire (Fig. 3f). This confirms the high conductivity of Li metal and the continuity of the Li deposition inside the nanotube. Moreover, the a-C shells also allow Li ions to diffuse across neighboring nanotubes, as demonstrated by the rapid filling of Li inside the hollow cavities of multiple Au@aCNTs contacted with each other (Fig. S5 and Video S2). The efficient inter-tube ion transport would be beneficial for uniform Li plating in the deeper interior of a host far from the electrolyte.

Supplementary data related to this article can be found at https://doi.org/10.1016/j.nanoen.2019.104178.

The Au-seeded growth of Li is highly related to the Au–Li alloying reaction. However, the microscopic processes of this electrochemical-driven reaction, especially with the confinement of a host substrate, is yet to be elucidated. Therefore, *in situ* selected area electron diffraction (SAED) was employed. A reversible two-step phase conversion process during Au–Li alloying/dealloying was revealed, in accordance with the TEM observation of the morphological evolution in Fig. 2.

Fig. 4a shows the SAED pattern of an Au@aCNT with multiple metallic Au NPs inside. The diffraction rings from Li_2O would be visible throughout the reaction, as known for many in-situ TEM lithiation experiments (especially on carbon-based materials) [35,36]. Au particles are partially alloyed to form $LiAu_3$ due to the insufficient Li supply in the early stage of lithiation, as revealed in Fig. 4b [37,38]. Further lithiation leads to the formation of a Li-rich phase of Li_3Au (Fig. 4c). Eventually, Au completely transforms into Li_3Au upon full lithiation, coexisting with metallic Li (Fig. 4d). Thus, the phase conversion of Au upon lithiation is given as follows:

$$Au \rightarrow LiAu_3 \rightarrow Li_3Au \quad (1)$$

Here, the Au–Li alloying reaction involves an intermediate phases of $LiAu_3$, quite different from the previous work that reported Li_3Au only [39]. This can be partly attributed to the shell confinement that slows down the alloying reaction (Fig. 2f) and allows this transitional phase to be detectable. Although multiple Li_xAu phases might be involved according to the phase diagram, only two of them can be identified by our SAED analysis, consistent with a recent result obtained from XRD [40]. Moreover, the phase conversion from Au to $LiAu_3$ and Li_3Au should be accompanied by notable volume changes according to the ratio of 1: 1.23: 3.69 (Fig. S6), which is well supported by our TEM observation. As

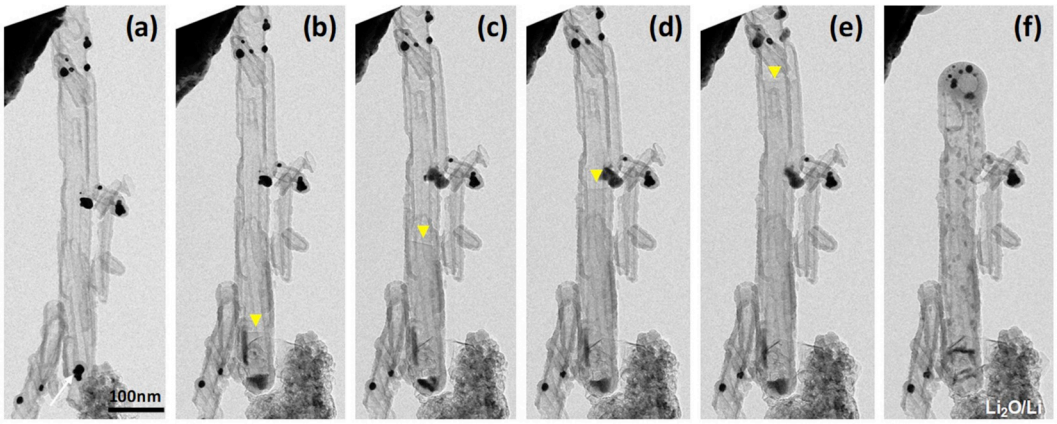

Fig. 3. Upward growth of Li inside an Au@aCNT and its electrical failure. (a) The pristine nanotube with a gold particle near the bottom (pointed by the white arrow) that initiates the Li deposition. (b–e) Upward propagation of the deposition front, as indicated by the yellow arrowheads. (f) The nanotube after the electrical breakdown caused by a short circuit once the nanotube cavity is fully filled with Li.

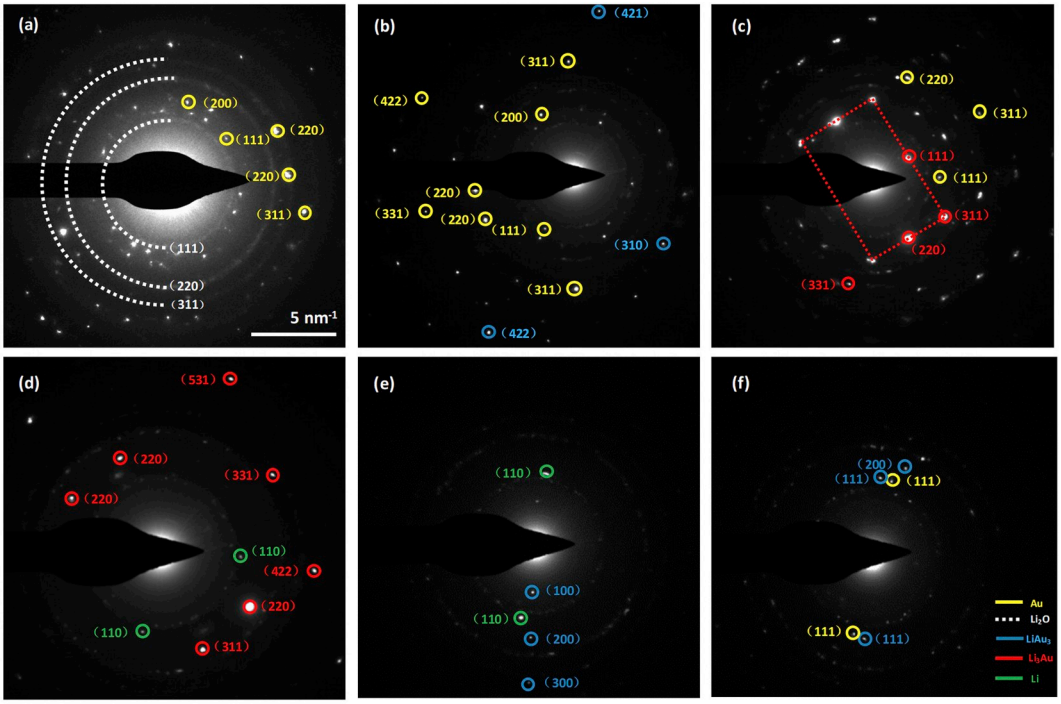

Fig. 4. Time-lapse diffraction patterns revealing the phase evolution of Au NPs in reaction with Li inside an Au@aCNT. (a) Pristine Au NPs in the nanotube. The diffraction rings indexed as Li_2O are visible throughout the whole cycle, and therefore not indexed in b-f. (b) Au alloying with Li in the early stage to form $LiAu_3$. (c) Formation of Li_3Au upon further alloying with Li. (d) Li metal deposition induced by Li_3Au (e) Reappearance of $LiAu_3$ during Li stripping/dealloying. (f) Reappearance of Au and disappearance of Li at the end of stripping.

seen in Fig. 2, for example, the alloyed Au seed goes through the slight (Fig. 2a_2) and then remarkable (Fig. 2a_3 and 2a_4) volume expansions.

The appearance of Li around the Li_3Au surface, as revealed by both TEM observation (Fig. 2a_3) and diffraction analysis (Fig. 4d), suggests that due to the lithiophilic nature, Li_3Au plays the actual role in inducing Li nucleation. In addition, the diffraction spots circled in green correspond to the (110) lattice planes of metallic Li, confirming the crystalline nature of the deposited Li. This is different from the previous report on the amorphous Li nuclei obtained by conventional Li deposition with liquid electrolytes [41]. The difference in the crystallinity of Li nuclei may arise from our special experimental conditions with dry-cell configuration and confined deposition space.

During stripping, Li_3Au is gradually converted into $LiAu_3$, while the metallic Li phase is still detectable (Fig. 4e). This can be explained by the stripping process observed in Fig. 2$a_{6\text{-}7}$, where the Li deposit keeps shrinking away from the above dealloying particle. In the final stage, $LiAu_3$ can be further dealloyed to form Au (at least partially), as revealed by the diffraction pattern in Fig. 4f, consistent with the observation of the contracted particle with a reduced size and darker contrast (Fig. 2a_8). Then, the reaction steps during Li_xAu dealloying can be described as (the exact reverse of its alloying process):

$$Li_3Au \rightarrow LiAu_3 \rightarrow Au \quad (2)$$

Nanotubes with Au NPs anchored on their outer surface can be occasionally found (Fig. S7a for more structural details). Due to the lack of spatial confinement, the outside particles would behave quite differently in the reaction with Li. We then chose an Au@aCNT with both inside and outside Au NPs for a comparative study of this issue, as shown in Fig. 5a.

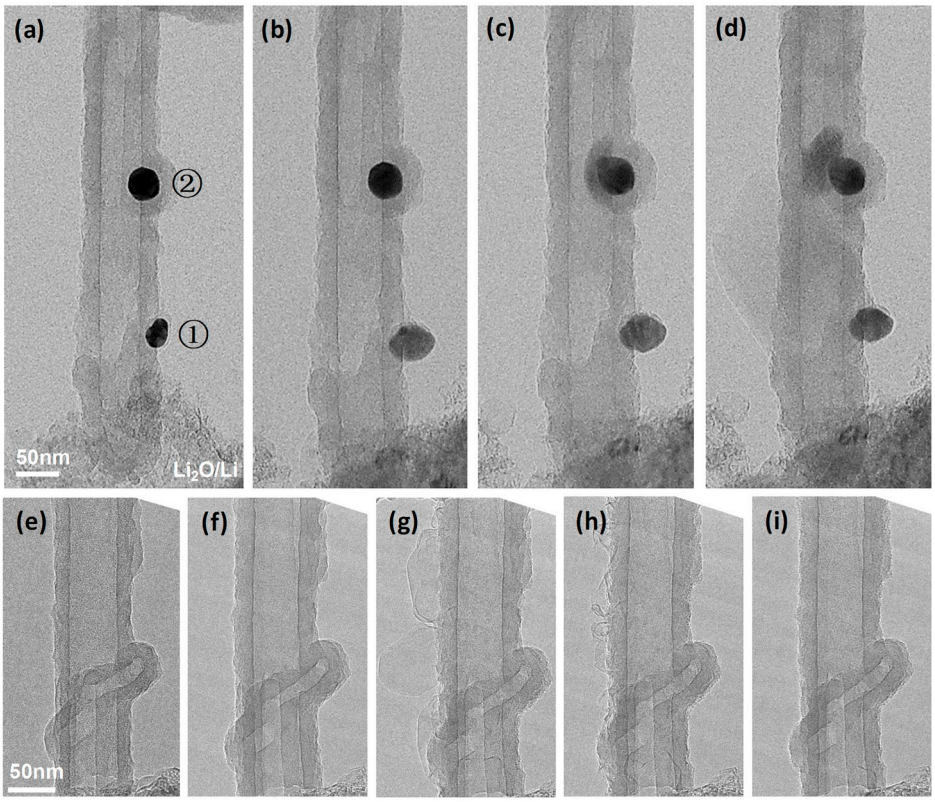

Fig. 5. Li deposition on Au@aCNTs with outside or no Au particles. (a) Pristine nanotube with two Au particles on its inner (particle 1) and outer (particle 2) surfaces, respectively. (b) Size expansion of Au NP 2 upon alloying with Li. (c) Size expansion of Au NP 1 hindered by the carbon shell upon lithiation. (d) Li deposition confined inside the nanotube induced by Au NP 1 and uncontrolled growth of a dendrite-like Li particle induced by Au NP 2. A pristine aCNT (e) undergoes shell expansion (f) and Li dendrite growth on its outer surface during plating (g), and the deposited Li particles shrinks in size (h) and are completely removed from the nanotube after stripping (i).

As expected, the outer Au NP (particle 1) expanded in size freely upon lithiation, whereas the inner one (particle 2) remained almost unchanged in the early stage (Fig. 5b). Li first nucleated on the outer alloyed particle, resulting in rapid growth of a large Li crystal exceeding the nanotube diameter (Fig. 5d). This result further confirms the role of Au NPs in guiding Li deposition. Meanwhile, it implies that the uncontrolled Li growth outside the nanotubes may develop into dendrites (if upon further plating) without shell confinement. In comparison, the reaction of the inner Au particle with Li was significantly retarded due to the confinement effect (as illustrated in Fig. 2f). As shown in Fig. 5b, the inward expansion of the particle 2 seems to be hindered. Upon further lithiation, the gold particle started to enter the inner space of the nanotube under high extrusion pressure caused by particle expansion (Fig. 5c). This partially alloyed gold seed then initiated the Li deposition inside the nanotube cavity (Fig. 5d), the same as the "active" particle 1 in Fig. 2.

To further verify the role of gold NPs in guiding Li deposition inside the tube cavity, amorphous CNTs without gold NPs were also used as the host for Li plating/stripping. Fig. 5e shows a pristine aCNT with its open end in contact with a Li_2O/Li electrode. After full lithiation, the tube diameter increased from 86.4 nm to 100 nm by 16%, accompanied with a shell thickening from 17.3 nm to 22.8 nm by 32% (Fig. 5f). Upon further plating, a number of Li dendrites grown outside the carbon shell were observed (Fig. 5g). Clearly, without the guidance of Au NPs, Li deposition tends to occur outside a nanotube, even though the tube end is open. During stripping, the outside Li crystals shrank slowly leaving the Li_2O shells behind (Fig. 5h). Unexpectedly, these Li_2O layers can be completely removed from the tube surface during prolonged stripping (Fig. 5i and Video S3). It would be interesting to compare our results with those of the well-crystalline multiwalled CNTs (MWCNTs). The in-situ lithiated MWCNTs become remarkably distorted and brittle, and the coating layer of Li_2O is hard to remove after delithiation [36]. In contrast, due to the amorphous nature, our aCNTs are rather robust during cycling without obvious structural degradation. The a-C shell also provides the channels for efficient ion transport, enabling a highly reversible plating/stripping process.

Supplementary data related to this article can be found at https://doi.org/10.1016/j.nanoen.2019.104178.

Recently, battery systems based on other alkali metals, such as sodium, have been intensively studied owing to their high natural abundance and low cost [42–45]. Similarly, controlled Na deposition through heterogeneous seeded growth becomes increasingly important for creating high-performance Na metal anodes [42, 46–50]. Therefore, it is worth exploring the possibility of both Au-seeded Na deposition and its encapsulation inside nanocapsules. Herein, we made a pioneering attempt by using Au@aCNTs as the Na deposition host.

Despite the larger radius than Li^+, Na ions are also permitted to penetrate the amorphous carbon shell and react with the inside Au NPs, as evidenced by the gold particles 1–4 that are sequentially sodiated according to their distance to the Na_2O/Na electrode (Fig. 6 and Video S4). Na ions from the Na_2O/Na electrode first reacted with Au NP 1 at the tube bottom, inducing the Na deposition inside the nanotube (Fig. 6b). The deposition front (as highlighted by the yellow dashed line) propagated upward, and before its arrival, Au NP 2 was sodiated as the result of Na ion transport along the tube wall (Fig. 6c). This particle was then partially dissolved into the growing Na metal, followed by immediate phase segregation that resulted in mass expansion of the alloyed particle at the tube bottom (Fig. 6d). The upper Au NPs 3 and 4 were sodiated later and completely (NP 3) or partially (NP 4) dissolved into the metallic Na, leading to the further segregation and accumulation of Na_xAu alloys (see Ref. [51] or Fig. S4 for the binary phase diagram) [51] at the tube bottom (Fig. 6e and f). During stripping, the Na deposition front retreated backward gradually (Fig. 6g). At the end of this cycle, the bottom particle also experienced a size contraction upon dealloying (Fig. 6h), similar to the Li stripping processes. Note that Au NP 5 also behaves like a "dead" particle as discussed above, which remains almost unchanged throughout the cycle due to the rigid shell confinement.

Supplementary data related to this article can be found at https

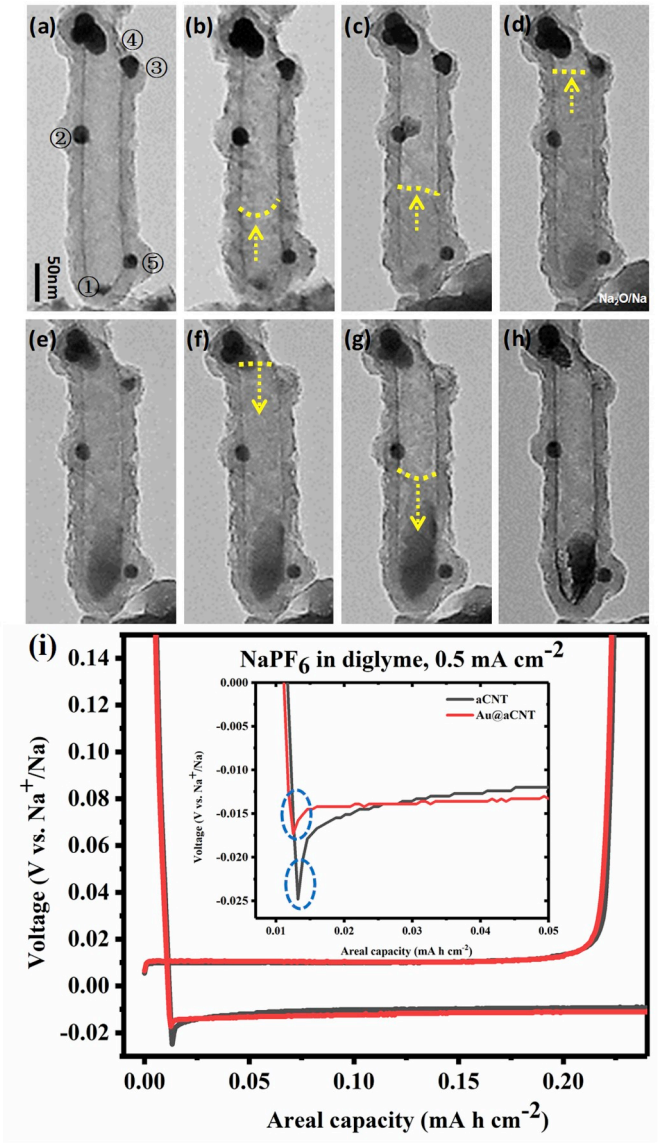

Fig. 6. Encapsulation of sodium metal in an Au@aCNT. Time-lapse TEM snapshots showing a full cycle of Na deposition/stripping inside an Au@aCNT. The Au NPs 1–4 are sequentially sodiated in numerical order, and the deposition fronts are highlighted by the yellow arrowheads. (a) Pristine Au@aCNT. (b) Inside Li deposition induced by Au 1. (c) Size expansion of Au NP 2 upon sodiation. Sodiation/dissolution of Au NP 3 (d) and NP 4 (e). (f) Full dissolution of Au NP 3 into Na metal in the beginning of stripping. Shrinkage of the deposited Na (g) and the Na/Au alloyed particle (h) during stripping. (i) Voltage profiles of Au@aCNTs and aCNTs during Na plating/stripping at a current density of 0.5 mA cm^{-2}. The inset shows the enlarge voltage profiles, with the overpotential circled by the dashed lines.

://doi.org/10.1016/j.nanoen.2019.104178.

We also compared the nucleation potential of Na on the amorphous CNTs with and without NPs inside. As shown in Fig. 6i, the nanotubes without NPs loaded exhibit an appreciable overpotential of 11.7 mV at 0.5 $mAcm^{-2}$, whereas the overpotential of Au@aCNTs is observable but very small (3.5 mV), further confirming the role of Au seeds in guiding Na deposition due to the lower nucleation barrier.

3. Conclusions

To conclude, we have fabricated the Au@aCNT hosts to study the Au-seeded Li/Na plating and striping kinetic processes confined in a one-dimensional space by in-situ TEM. By comparing the Li deposition behaviors in three different amorphous CNTs that have inside, outside or no Au particles respectively, we confirm the dominant role of Au NPs in guiding Li growth inside the nanotube hollow cavity. A reversible two-step phase conversion is revealed during Au–Li alloying/dealloying reactions, and Li nucleation is highly dependent on the formation of Li_3Au. A scenario is proposed to explain the confined Li growth and stripping kinetics, which involves the ion diffusion along the tube wall and atom addition and removal at the deposition front. We also demonstrate that Au-seed growth is effective in encapsulating sodium inside the nanotube cavity. These results would be particularly important for Li/Na anode host design based on heterogeneous seeded Li/Na growth and spatial-control deposition.

4. Experimental section

4.1. Preparation of Au@aCNTs

The sacrificial template ZnO nanowires (prepared via a modified method according to the previous literature [52]) were dispersed in 150 ml ethanol by sonication. The solution was added with 1 ml (3-aminopropyl) triethoxysilane (APTES, Aldrich), followed by stirring overnight. The as-obtained ZnO nanowires were collected by filtration, washed with ethanol for several times, and then redispersed in 20 ml ethanol by sonication. Gold nanoparticles (NPs) were prepared via a classic recipe with the use of chloroauric acid ($HAuCl_4$, Aldrich) [53]. The obtained suspension was mixed with the former solution, and the ZnO nanowires decorated with gold NPs were collected by filtration. The ZnO@Au nanowires were coated with formaldehyde resin [54], and then carbonized under Ar_2 atmosphere at 600 °C for 4 h. The ZnO template can be removed simply by hydrochloric acid (HCl, Aladin, 1 M) etching for 6 h. The obtained sample was filtered and washed with ethanol by vacuum filtration. The solid Au@aCNTs product was collected and dried in a vacuum oven at 60 °C for 24 h before use. The hollow amorphous CNTs without Au NPs were prepared in a similar procedure as the control sample.

4.2. Material characterization

The morphology and microstructure of the as-prepared samples were studied by high-resolution TEM, STEM-HADDF, EDS elemental mapping and selected area electron diffraction (SAED) with a transmission electron microscope (FEI, Talos 200s) operating at 200 kV.

4.3. Electrode preparation and deposition overpotential test on Au@aCNTs

Coin cells (CR2025) were assembled in an argon-filled glove box. The working electrode was prepared by mixing Au@aCNTs, carbon black (Super P) and polyvinylidene difluoride binder (PVDF) with a mass ratio of 8:1:1 in N-methylpyrrolidone overnight (NMP, Aldrich) to form a slurry. After casting the slurry onto a copper foil (d = 1.4 cm) with a doctor blade, the electrode was dried in vacuum oven overnight. Lithium foil was used as counter electrode, and Celguard 2300 serve as separator. The electrolyte contained 1.0 M LiPF6 in (EC), diethyl carbonate membrane (DEC) and dimethyl carbonate (DMC) (1:1:1 vol ratio) with 10 vol % fluoroethylene carbonate. The overpotential test was carried out on a NEWARE multi-channel battery test system. The discharge time was fixed for limited capacity of 0.25 mA h cm^{-2} in the lithium plating process, and the charge time during stripping process was controlled by a cut-off voltage of 0.5 V. The charge/discharge was fixed with a desirable current density of 0.5 mA cm^{-2}. The mass loading of the active material was about 0.3 mg cm^{-2}. For the deposition overpotential test of sodium on Au@aCNT electrodes, sodium foil was used as counter electrode, and 1.0 M NaPF6 in diglyme as the electrolyte.

4.4. In situ TEM characterization

A typical nanoscale open-cell battery setup was constructed inside a TEM (FEI, Talos F200s) by using a STM holder, which is capable of piezo-driven manipulation and electrical biasing. The Au@aCNTs were attached on a gold wire for use as the working electrode. A movable tungsten tip loaded with a tiny amount of Li metal served as counter electrode, and its surface Li_2O as a solid electrolyte. After the Li_2O/Li electrode was brought into contact with a single Au@aCNT, a constant bias of −3.0 V/3.0 V was applied to the nanotube against Li metal to initiate the Li plating/stripping processes. In-situ TEM experiments on sodium were performed in a similar way by using sodium instead of Li as the counter electrode.

Declaration of competing interest

The authors declare that they have no known competing financial interests or personal relationships that could have appeared to influence the work reported in this paper.

Acknowledgements

The authors would like to thank Jinming Wang of Xiamen University in China for a technical support in the course of this work. This work was financially supported by the National Natural Science Foundation of China (Nos. 61471307, 51871188), the Specialized Research Fund for the Doctoral Program of Higher Education (No. 20130121120009), the Fundamental Research Funds for the Central Universities, National Program for Thousand Young Talents of China, and the "Double-First Class" Foundation of Materials and Intelligent Manufacturing Discipline of Xiamen University.

Appendix A. Supplementary data

Supplementary data to this article can be found online at https://doi.org/10.1016/j.nanoen.2019.104178.

References

[1] Y. Guo, H. Li, T. Zhai, Adv. Mater. 29 (29) (2017).
[2] D. Lin, Y. Liu, Y. Cui, Nat. Nanotechnol. 12 (3) (2017) 194–206.
[3] B. Liu, J.-G. Zhang, W. Xu, Joule 2 (5) (2018) 833–845.
[4] J.M. Zheng, J.A. Lochala, A. Kwok, Z.Q.D. Deng, J. Xiao, Adv. Sci. 4 (8) (2017).
[5] G. Zheng, S.W. Lee, Z. Liang, H.W. Lee, K. Yan, H. Yao, H. Wang, W. Li, S. Chu, Y. Cui, Nat. Nanotechnol. 9 (8) (2014) 618–623.
[6] L.L. Li, S.Y. Li, Y.Y. Lu, Chem. Commun. 54 (50) (2018) 6648–6661.
[7] X.B. Cheng, T.Z. Hou, R. Zhang, H.J. Peng, C.Z. Zhao, J.Q. Huang, Q. Zhang, Adv. Mater. 28 (15) (2016) 2888–2895.
[8] L.L. Lu, J. Ge, J.N. Yang, S.M. Chen, H.B. Yao, F. Zhou, S.H. Yu, Nano Lett. 16 (7) (2016) 4431–4437.
[9] L. Li, S. Basu, Y. Wang, Z. Chen, P. Hundekar, B. Wang, J. Shi, Y. Shi, S. Narayanan, N. Koratkar, Science 359 (6383) (2018) 1513–1516.
[10] H. Ye, S. Xin, Y.X. Yin, J.Y. Li, Y.G. Guo, L.J. Wan, J. Am. Chem. Soc. 139 (16) (2017) 5916–5922.
[11] Y. Zhang, C. Wang, G. Pastel, Y. Kuang, H. Xie, Y. Li, B. Liu, W. Luo, C. Chen, L. Hu, Adv. Energy Mater. 8 (18) (2018).
[12] Z.H. Wang, X.D. Wang, W. Sun, K.N. Sun, Electrochim. Acta 252 (2017) 127–137.
[13] B.D. Adams, E.V. Carino, J.G. Connell, K.S. Han, R.G. Cao, J.Z. Chen, J.M. Zheng, Q.Y. Li, K.T. Mueller, W.A. Henderson, J.G. Zhang, Nano Energy 40 (2017) 607–617.
[14] S. Liu, A. Wang, Q. Li, J. Wu, K. Chiou, J. Huang, Luo, J. Joule 2 (1) (2018) 184–193.
[15] R. Mukherjee, A.V. Thomas, D. Datta, E. Singh, J. Li, O. Eksik, V.B. Shenoy, N. Koratkar, Nat. Commun. 5 (2014) 3710.
[16] G.Y. Zheng, S.W. Lee, Z. Liang, H.W. Lee, K. Yan, H.B. Yao, H.T. Wang, W.Y. Li, S. Chu, Y. Cui, Nat. Nanotechnol. 9 (8) (2014) 618–623.
[17] D. Lin, Y. Liu, Z. Liang, H.W. Lee, J. Sun, H. Wang, K. Yan, J. Xie, Y. Cui, Nat. Nanotechnol. 11 (7) (2016) 626–632.
[18] C. Niu, H. Pan, W. Xu, J. Xiao, J.G. Zhang, L. Luo, C. Wang, D. Mei, J. Meng, X. Wang, Z. Li, L. Mai, J. Liu, Nat. Nanotechnol. 14 (6) (2019) 594.
[19] Z. Huang, G. Zhou, W. Lv, Y. Deng, Y. Zhang, C. Zhang, F. Kang, Q.-H. Yang, Nano Energy 61 (2019) 47–53.
[20] K. Yan, Z. Lu, H.-W. Lee, F. Xiong, P.-C. Hsu, Y. Li, J. Zhao, S. Chu, Y. Cui, Nat. Energy 1 (3) (2016).
[21] T.T. Zuo, Y.X. Yin, S.H. Wang, P.F. Wang, X. Yang, J. Liu, C.P. Yang, Y.G. Guo, Nano Lett. 18 (1) (2018) 297–301.
[22] H. Wang, Y. Li, Y. Li, Y. Liu, D. Lin, C. Zhu, G. Chen, A. Yang, K. Yan, H. Chen, Y. Zhu, J. Li, J. Xie, J. Xu, Z. Zhang, R. Vila, A. Pei, K. Wang, Y. Cui, Nano Lett. 19 (2) (2019) 1326–1335.
[23] C.P. Yang, Y.G. Yao, S.M. He, H. Xie, E. Hitz, L.B. Hu, Adv. Mater. 29 (38) (2017).
[24] H.L. Fan, C.H. Gao, Q.Y. Dong, B. Hong, Z. Fang, M.Y. Hu, Y.Q. Lai, J. Electroanal. Chem. 824 (2018) 175–180.
[25] Q.D. Sun, W. Zhai, G.M. Hou, J.K. Feng, L. Zhang, P.C. Si, S.R. Guo, L.J. Ci, ACS Sustain. Chem. Eng. 6 (11) (2018) 15219–15227.
[26] P.B. Zhai, T.S. Wang, W.W. Yang, S.Q. Cui, P. Zhang, A.M. Nie, Q.F. Zhang, Y. J. Gong, Adv. Energy Mater. 9 (18) (2019).
[27] K. Xu, M. Zhu, X. Wu, J. Liang, Y. Liu, T. Zhang, Y. Zhu, Y. Qian, Energy Storage Mater. (2019). https://doi.org/10.1016/j.ensm.2019.03.025.
[28] Y. Liu, F.F. Fan, J.W. Wang, Y. Liu, H.L. Chen, K.L. Jungjohann, Y.H. Xu, Y.J. Zhu, D. Bigio, T. Zhu, C.S. Wang, Nano Lett. 14 (6) (2014) 3445–3452.
[29] N. Liu, Z.D. Lu, J. Zhao, M.T. McDowell, H.W. Lee, W.T. Zhao, Y. Cui, Nat. Nanotechnol. 9 (3) (2014) 187–192.
[30] L. Zhao, H.H. Wu, C. Yang, Q. Zhang, G. Zhong, Z. Zheng, H. Chen, J. Wang, K. He, B. Wang, T. Zhu, X.C. Zeng, M. Liu, M.S. Wang, ACS Nano 12 (12) (2018) 12597–12611.
[31] X.K. Li, L.Z. Zhao, P. Li, Q.B. Zhang, M.S. Wang, Nano Energy 42 (2017) 122–128.
[32] A.D. Pelton, Bull. Alloy Phase Diagr. 7 (3) (1986) 228–231.
[33] S.Y. Pung, K.L. Choy, X.H. Hou, J. Cryst. Growth 312 (14) (2010) 2049–2055.
[34] Dresselhaus, M. S.; Dresselhaus, G.; Avouris, P. Springer-Verlag: Berlin, 2001, Ch. 4.
[35] X.H. Liu, J.W. Wang, Y. Liu, H. Zheng, A. Kushima, S. Huang, T. Zhu, S.X. Mao, J. Li, S. Zhang, W. Lu, J.M. Tour, J.Y. Huang, Carbon 50 (10) (2012) 3836–3844.
[36] Y. Liu, H. Zheng, X.H. Liu, S. Huang, T. Zhu, J. Wang, A. Kushima, N.S. Hudak, X. Huang, S. Zhang, S.X. Mao, X. Qian, J. Li, J.Y. Huang, ACS Nano 5 (9) (2011) 7245–7253.
[37] Y.J. Lee, Y. Lee, D. Oh, T. Chen, G. Ceder, A.M. Belcher, Nano Lett. 10 (7) (2010) 2433–2440.
[38] Z. Zeng, W.I. Liang, Y.H. Chu, H. Zheng, Faraday Discuss 176 (2014) 95–107.
[39] X. Ke, Y. Liang, L. Ou, H. Liu, Y. Chen, W. Wu, Y. Cheng, Z. Guo, Y. Lai, P. Liu, Z. Shi, Energy Storage Mater. (2019). https://doi.org/10.1016/j.ensm.2019.04.003.
[40] X.J. Shen, G.Y. Zhao, K.N. Sun, Electrochim. Acta 317 (2019) 333–340.
[41] X. Wang, M. Zhang, J. Alvarado, S. Wang, M. Sina, B. Lu, J. Bouwer, W. Xu, J. Xiao, J.G. Zhang, J. Liu, Y.S. Meng, Nano Lett. 17 (12) (2017) 7606–7612.
[42] A.P. Cohn, N. Muralidharan, R. Carter, K. Share, C.L. Pint, Nano Lett. 17 (2) (2017) 1296–1301.
[43] W. Luo, Y. Zhang, S.M. Xu, J.Q. Dai, E. Hitz, Y.J. Li, C.P. Yang, C.J. Chen, B.Y. Liu, L.B. Hu, Nano Lett. 17 (6) (2017) 3792–3797.
[44] S. Xin, Y.X. Yin, Y.G. Guo, L.J. Wan, Adv. Mater. 26 (8) (2014) 1261–1265.
[45] S. Wei, S. Xu, A. Agrawral, S. Choudhury, Y. Lu, Z. Tu, L. Ma, L.A. Archer, Nat. Commun. 7 (2016) 11722.
[46] M.Q. Zhu, S.M. Li, B. Li, Y.J. Gong, Z.G. Du, S.B. Yang, Sci. Adv. 5 (4) (2019).
[47] Z.J. Zheng, X.X. Zeng, H. Ye, F.F. Cao, Z.B. Wang, ACS Appl. Mater. Interfaces 10 (36) (2018) 30417–30425.
[48] J.M. Luo, C.L. Wang, H. Wang, X.F. Hu, E. Matios, X. Lu, W.K. Zhang, X.Y. Tao, W. Y. Li, Adv. Funct. Mater. 29 (3) (2019).
[49] H. Ye, C.Y. Wang, T.T. Zuo, P.F. Wang, Y.X. Yin, Z.J. Zheng, P. Wang, J. Cheng, F. F. Cao, Y.G. Guo, Nano Energy 48 (2018) 369–376.
[50] B. Sun, P. Li, J. Zhang, D. Wang, P. Munroe, C. Wang, P.H.L. Notten, G. Wang, Adv. Mater. (2018), e1801334.
[51] A.D. Pelton, Bull. Alloy Phase Diagr. 7 (2) (1986) 136–139.
[52] B. Cheng, E.T. Samulski, Chem. Commun. (Camb) (8) (2004) 986–987.
[53] G. Frens, Nat. Phys. Sci. (Lond.) 241 (105) (1973) 20.
[54] N. Li, Q. Zhang, J. Liu, J. Joo, A. Lee, Y. Gan, Y.D. Yin, Chem. Commun. 49 (45) (2013) 5135–5137.

Xiangna Lan received her B.E. degree from the Department of Materials Science and Engineering, College of Materials at Xihua University. Currently, she is a Master student at the Department of Materials Science and Engineering of Xiamen University under the supervision of Prof. Ming-Sheng Wang. Her research focuses on the design and in-situ TEM investigation of anode materials for Li/Na metal batteries.

Weibin Ye is currently a Ph.D. candidate at the Department of Materials Science and Engineering of Xiamen University under the supervision of Prof. Ming-Sheng Wang. His research focuses mainly on the study of the lithiophilic chemistry and material design for Li metal anodes by in-situ electron microscopies.

Hongfei Zheng received his B.E. degree from Department of Materials Science and Engineering, College of Materials, Xiamen University. Currently, he is a Ph.D. candidate in Department of Materials Science and Engineering of Xiamen University under the supervision of Prof. Dong-Liang Peng. His research focuses on the design and synthesis of high-performance electrode nanomaterials for energy storage.

Yong Cheng is currently a Ph.D. candidate under the supervision of Prof. Ming-Sheng Wang at the Department of Materials Science and Engineering, Xiamen University. His research interests focus on the structural and physical properties tuning of carbon materials by *in situ* TEM and in-situ characterization of anode materials for alkali metal ion batteries.

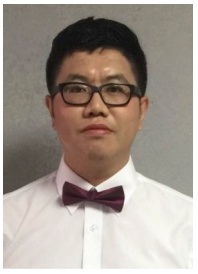

Qiaobao Zhang is currently an Assistant Professor in the Department of Materials Science and Engineering at Xiamen University. He obtained his M.S. degree from Xiamen University in 2010 and Ph.D. degree from City University of Hong Kong (supervised by Prof Kaili Zhang) in 2016. He joined Prof. Meilin Liu's group as a visiting Ph.D. student in Georgia Institute of Technology in 2015. His current research includes developing nanostructured materials for electrochemical energy storage devices such as Li/Na ion batteries and supercapacitors and investigating their energy storage mechanism by *in situ* SEM/TEM. His research results have been published in Progress in Materials Science, Energy & Environmental Science, Advanced Energy Materials, ACS Nano, Nano Letters, Nature Communications, Science Advances, Nano Energy, Energy Storage Materials, Small, Journal of Materials Chemistry A, etc.

Dong-Liang Peng is Chair Professor of Materials Science and Engineering at Xiamen University. He received his B.S. (1983), M.S. (1989) and Ph.D. (1997) in Condensed Matter Physics from Lanzhou University. He also received Ph.D. degree in Materials Science and Engineering from Nagoya Institute of Technology (Japan) in 2002. He became a professor of College of Materials in Xiamen University in 2005. He is an editor of Journal of Materials Science: Materials in Electronics. His research focuses on the development of new methodologies for the synthesis of nano and low-dimensional functional materials, as well as their applications in catalysis, energy conversion/storage and electromagnetics.

Mingsheng Wang is currently a Professor at Xiamen University, and he leads the advanced electron microscopy group in the college of materials. He received his Bachelor's degree in Physics from Nanjing University in 2001 and PhD degree in Physical Electronics from Peking University in 2006. He did his postdoctoral research at the National Institute for Materials Science in Japan and Massachusetts Institute of Technology from 2008 to 2012. His research interests concentrate on in-situ electron microscopy and its application in sp^2 carbon-based nanotechnology, as well as the design and fabrication of high-performance energy storage devices based on low-dimensional material architectures (group website: http://mswang.xmu.edu.cn).